

# **A Comprehensive Quantum Cascade Laser Model**

Muhammad A. Talukder, Curtis R. Menyuk, and Fow-Sen Choa

Department of Computer Science and Electrical Engineering

University of Maryland, Baltimore County

1000 Hilltop Circle, Baltimore, MD 21250

email: [anisuzzaman@umbc.edu](mailto:anisuzzaman@umbc.edu)

# Contents

<b>1</b>	<b>Energy Values and Wavefunctions</b>	<b>2</b>
1.1	Finte Difference Scheme . . . . .	2
1.1.1	MATLAB routines . . . . .	3
1.1.2	Infinite Single Quantum Well . . . . .	3
1.1.3	Finite Single Quantum Well . . . . .	4
1.2	Extension to Variable Effective Mass . . . . .	5
1.3	Band Non-parabolicity Effects . . . . .	7
1.4	Poisson's Equation . . . . .	10
1.4.1	Calculating $V_\rho(z)$ . . . . .	10
1.4.2	Self-consistent Schrödinger-Poisson Solution . . . . .	12
<b>2</b>	<b>Intersubband Transitions</b>	<b>15</b>
2.1	Dipole Matrix Element . . . . .	15
2.2	Nonradiative Transitions . . . . .	17
2.2.1	Fermi's Golden Rule . . . . .	17
2.2.2	Polar Longitudinal Optical (LO) Phonon Scattering . . . . .	17
2.2.3	Electron-Electron Scattering . . . . .	21

# Chapter 1

## Energy Values and Wavefunctions

### 1.1 Finite Difference Scheme

We start with the time-independent constant-mass Schrödinger equation [1], the analytical solutions of which are possible in some limited cases,

$$-\frac{\hbar^2}{2m^*} \frac{\partial^2}{\partial z^2} \psi(z) + V(z)\psi(z) = E\psi(z), \quad (1.1)$$

where  $V(z)$  is the one-dimensional band-edge potential,  $\psi(z)$  is the wavefunction representing the particle of interest within the effective mass and envelope function approximations,  $m^*$  is the effective mass of an electron, and  $E$  is the eigenenergy. In the finite difference technique that we will employ, differential operators are replaced by difference equations. Using a finite difference expression for the second derivative, equation (1.1) can be written as

$$-\frac{\hbar^2}{2m^*} \left[ \frac{\psi(z + \Delta z) - 2\psi(z) + \psi(z - \Delta z)}{(\Delta z)^2} \right] + V(z)\psi(z) = E\psi(z). \quad (1.2)$$

We obtain after rearrangement

$$-\frac{\hbar^2}{2m^*} \left\{ \frac{\psi(z + \Delta z)}{(\Delta z)^2} - \left[ \frac{2}{(\Delta z)^2} + \frac{2m^*}{\hbar^2} V(z) \right] \psi(z) + \frac{\psi(z - \Delta z)}{(\Delta z)^2} \right\} = E\psi(z). \quad (1.3)$$

Equation (1.3) can be written as  $\mathbf{A}\psi = E\psi$ , which is a matrix eigenvalue problem. We solve equation (1.3) for the eigenfunctions (wavefunctions,  $\psi$ ) and eigenvalues (energy values,  $E$ ). Here, the operator matrix  $\mathbf{A}$  is a large tri-diagonal matrix. Built-in MATLAB routines can be used to solve this eigenvalue problem efficiently with high precision [2].

### 1.1.1 MATLAB routines

We specially use two matlab routines – **spdiags** to create the large tridiagonal matrix and **eigs** to determine its eigenfunctions and eigenvalues.

**spdiags** – creates a sparse matrix.

$A = \text{spdiags}(B, d, m, n)$  creates an  $m$ -by- $n$  sparse matrix by taking the columns of  $B$  and placing them along the diagonals specified by  $d$ .

**eigs** – determines the eigenfunctions and eigenvalues.

$[v, d] = \text{eigs}(A, B, k, \text{sigma}, \text{opts})$  where  $A$  is the sparse matrix,  $B$  is the identity matrix of the same size as  $A$ , and  $k$  is the maximum number of eigenvalues that will be obtained. The eigenvalues that are closest to  $\text{sigma}$  are found and  $\text{opts}$  can be used to set the convergence limit.

The wavefunctions obtained from this numerical method are not normalized, therefore, we normalize the wavefunctions to satisfy the condition

$$\sum_{j=1}^N \psi^*(z_j) \psi(z_j) \Delta z = 1, \quad (1.4)$$

where  $N$  is the number of node points in the finite-difference discretization and  $z_j$  is the  $j$ -th  $z$ -value discretization.

### 1.1.2 Infinite Single Quantum Well

We apply this computational approach for solving the Schrödinger equation to an infinitely deep quantum well for which analytical solution is available. We study a 10 nm GaAs infinite quantum well both analytically and computationally. Figure 1.1 shows the infinite quantum well and its wavefunctions and energy values. For the computational solution, we use a grid size of  $2\text{\AA}$ , so that  $N = 51$ . We compare the computationally-obtained energy values with those obtained using the analytical formula in Table 1. For the wavefunctions, the solid lines in the Fig. 1.1 represent the analytical solutions and the markers represent the computational solutions. In this example, we find that the error in the energy levels is less than 1%.

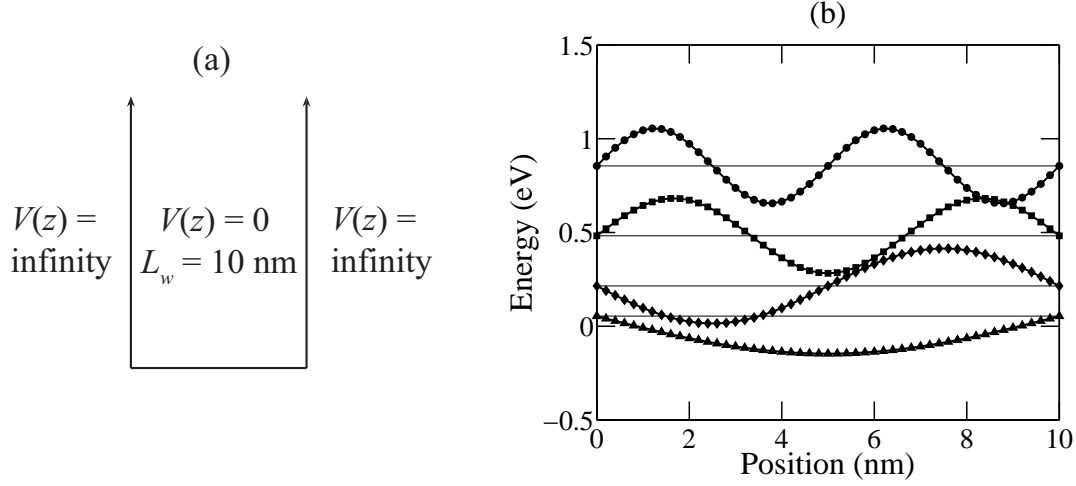


Figure 1.1: (a) Schematic illustration of a 10 nm GaAs infinite quantum well (b) Normalized wavefunctions and their energies for the infinite quantum well

Energy values	Analytical (meV)	Numerical (meV)
$E_1$	53.7	53.7
$E_2$	214.9	214.6
$E_3$	483.5	482.0
$E_4$	859.5	855.0

Table 1. Comparison of analytical and numerical calculated energy values

### 1.1.3 Finite Single Quantum Well

We calculate the energy values and the wavefunctions for an InGaAs quantum well having InAlAs barriers in both sides. The conduction band offset for the two materials used in the calculation is 0.52 eV. The well width is 60 Å and barrier width in each side is 100 Å. The calculated ground and first excited state wavefunctions are given in Fig. 1.2. We have calculated the energy values with different grid sizes until a reduction in the grid size does not make a significant change in the calculated values. With a grid size of 1 Å we get less than 0.25% error. The calculated energy eigenvalues with 1 Å grid size are:  $E_1 = 0.0817$  eV,  $E_2 = 0.3090$  eV.

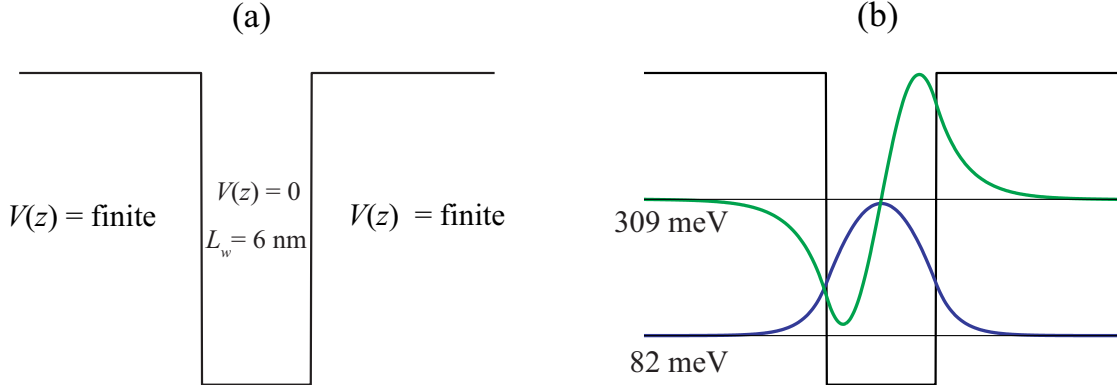


Figure 1.2: (a) One-dimensional single finite quantum well and (b) calculated energy values and wavefunctions for the InGaAs quantum well with InAlAs barriers

## 1.2 Extension to Variable Effective Mass

In the previous section, the effective masses of the electrons in the barrier and well materials were set equal. However, the electron effective masses are actually different for the materials used in the barrier and well. In this section we discuss the changes in the Schrödinger equation that must be implemented to account for different effective masses. We also discuss the effects of the different effective masses on the results.

The Schrödinger equation with a varying effective mass is given by

$$-\frac{\hbar^2}{2} \frac{\partial}{\partial z} \left[ \frac{1}{m^*(z)} \frac{\partial}{\partial z} \psi(z) \right] + V(z) \psi(z) = E \psi(z), \quad (1.5)$$

which may also be written as

$$-\frac{\partial}{\partial z} \left[ \frac{1}{m^*(z)} \right] \left[ \frac{\partial}{\partial z} \psi(z) \right] - \frac{1}{m^*(z)} \frac{\partial^2}{\partial z^2} \psi(z) + \frac{2}{\hbar^2} V(z) \psi(z) = \frac{2}{\hbar^2} E \psi(z), \quad (1.6)$$

or

$$\left[ \frac{1}{[m^*(z)]^2} \frac{\partial}{\partial z} m^*(z) \right] \left[ \frac{\partial}{\partial z} \psi(z) \right] - \frac{1}{m^*(z)} \frac{\partial^2}{\partial z^2} \psi(z) + \frac{2}{\hbar^2} V(z) \psi(z) = \frac{2}{\hbar^2} E \psi(z). \quad (1.7)$$

Then writing the derivatives as finite differences, we obtain

$$\begin{aligned} -\frac{\psi(z + \Delta z)}{m^*(z + \frac{\Delta z}{2})} + \left[ \frac{1}{m^*(z + \frac{\Delta z}{2})} + \frac{1}{m^*(z - \frac{\Delta z}{2})} + \frac{2(\Delta z)^2}{\hbar^2} V(z) \right] \psi(z) \\ - \frac{\psi(z - \Delta z)}{m^*(z - \frac{\Delta z}{2})} = \frac{2(\Delta z)^2}{\hbar^2} E \psi(z), \end{aligned} \quad (1.8)$$

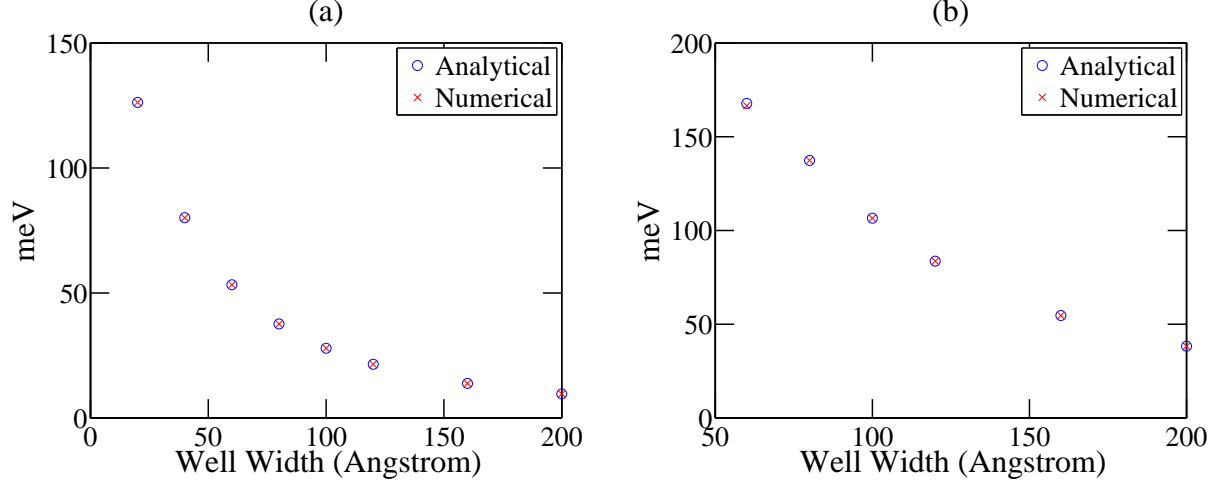


Figure 1.3: Comparison of the numerical solution with the analytical solution for a single quantum well with differing effective masses in the well and barrier for (a) the ground state and (b) the first excited state

The effective mass  $m^*$  at the intermediate points,  $z \pm \Delta z/2$ , is determined by taking the mean of the two neighboring points at  $z$  and  $z \pm \Delta z$ .

We calculate the ground and first excited energy levels for a GaAs quantum well surrounded by  $\text{Ga}_{0.8}\text{Al}_{0.2}\text{As}$  taking the different masses in the well and in the barrier into account. We vary the well thickness from 20–200 Å. The energy values have been calculated analytically for the same structure in Ref. 2. In Fig. 1.3 we compare our computationally calculated energy values with those calculated analytically in Ref. 2.

We study the effects of differing masses in comparison to constant mass. A single GaAs quantum well of 100 Å with  $\text{Ga}_{0.6}\text{Al}_{0.4}\text{As}$  barriers on both sides has been studied for the ground state. The ground state energy values have been calculated with different mass in well and barrier and with same mass in barrier and well, and have been plotted in Fig. 1.4. We see that ground state energy values, when different masses for well and barrier are considered are significantly smaller compared to the energy values when a fixed mass for well and barrier is considered.

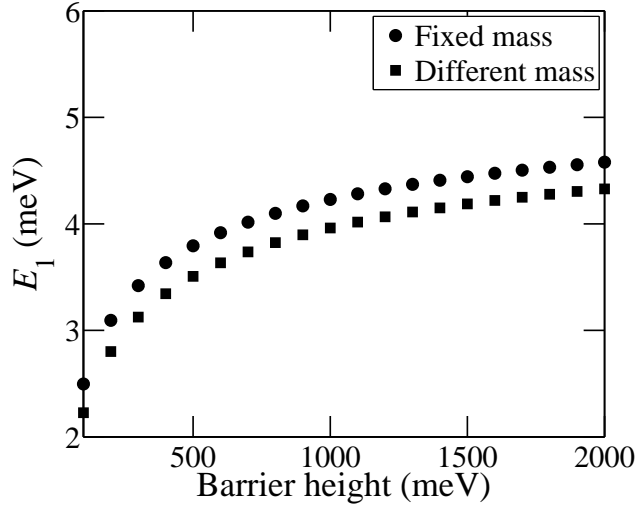


Figure 1.4: Electron ground state energy as a function of the barrier potential

### 1.3 Band Non-parabolicity Effects

For semiconductor heterostructures with lattice-matched GaAs/AlGaAs and InGaAs/InAlAs material systems that have a barrier height of only few hundreds meV and with a carrier density of  $< 10^{11} \text{ cm}^{-2}$ , the electrons cluster around the subband minima, specially at a low temperature, and their energy is within a couple of hundred meV of the bulk conduction band minima. In this parameter regime, the band minima, both the bulk conduction band and the in-plane subband, can be described by a parabolic  $E$ - $\mathbf{k}$  curve, *i.e.*, in the usual form

$$E = \frac{\hbar^2 |\mathbf{k}|^2}{2m^*}, \quad (1.9)$$

where  $\mathbf{k}$  can be read as a three-dimensional vector for the bulk, or as a two-dimensional in-plane vector  $|\mathbf{k}_{x,y}|$  for a subband.

However, in situations where the electrons are forced up to higher energies, *i.e.*,  $> 300$  meV, by either large barrier heights and narrow wells, or in the case of very high carrier densities, *i.e.*,  $> 10^{11} \text{ cm}^{-2}$ , Eq. (1.9) becomes more approximate. The same is true for holes in the valence band. The approximation can be improved upon by adding terms to the polynomial expansion for the energy. Since the basic definition of effective mass is given by

$$m^* = \hbar^2 \left( \frac{\delta^2 E}{\delta \mathbf{k}^2} \right)^{-1}, \quad (1.10)$$



we now find that  $m^*$  is a function of  $\mathbf{k}$ , unlike the case of parabolic bands where it is a constant. As it is a function of  $\mathbf{k}$ , it is also a function of energy, and indeed band non-parabolicity should be accounted for by allowing the effective mass to have an energy dependence.

Nonparabolicity in the neighborhood of energy-band extrema in bulk semiconductors can be described by the dispersion relation [4]

$$E = \frac{\hbar^2 \mathbf{k}^2}{2m^*} (1 - \gamma \mathbf{k}^2), \quad (1.11)$$

where  $\gamma$  is the nonparabolicity parameter.

The best and most basic way to handle nonparabolicity in quantum well structures is contained in the Bastard derivation [5], [6] of the envelope function approximation leading to a two-band (Kane) model. The Bastard treatment considers the interaction of the conduction band and light-hole valence band in both the well and barrier materials at once throughout the heterostructure. The heavy-hole valence band does not interact with these bands and possesses only a small nonparabolicity from interaction with other bands. The interband interaction produces the same effective mass  $m^*$  characterizing the parabolic response of each band and the same  $\gamma$  parameter characterizing the non-parabolicity of each band. When cast into the form of an energy-dependent effective-mass, this model applied to just one of the bands for a single quantum square well consists of the dispersion relation in the well [4]

$$E = \frac{\hbar^2 k_w^2}{2m_w^*(E)}. \quad (1.12)$$

The dispersion relation in the barrier is given by

$$E = V - \frac{\hbar^2 k_b^2}{2m_b^*(E)}, \quad (1.13)$$

and the boundary condition is given by

$$\left( \frac{k_w m_b^*(E)}{k_b m_w^*(E)} - \frac{k_b m_w^*(E)}{k_w m_b^*(E)} \right) \tan(k_w l) = 2. \quad (1.14)$$

Here the subscripts  $w$  and  $b$  denote well and barrier,  $k_w$  and  $k_b$  are the wave numbers for well and barrier,  $l$  is the well width,  $V$  is the energy barrier height at the interfaces, and the energy-dependent effective masses are given by

$$m_w^*(E) = m_w^* (1 + E/E_w), \quad (1.15)$$

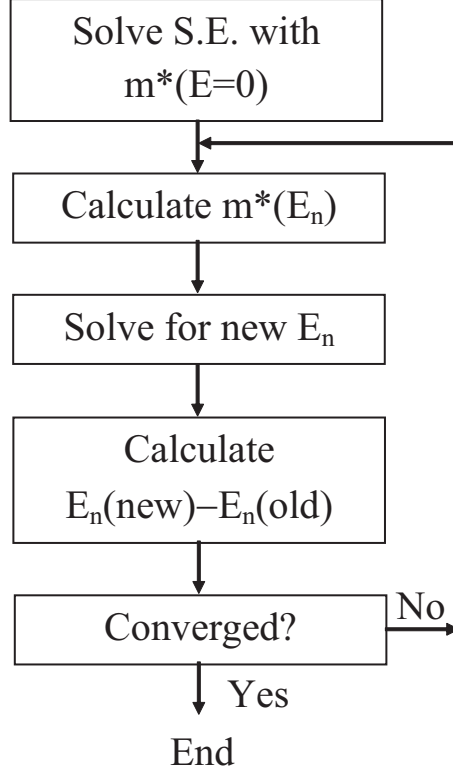


Figure 1.5: Block diagram of the implementation of band non-parabolicity

$$m_b^*(E) = m_b^* [1 - (V - E)/E_b], \quad (1.16)$$

where  $E_w$  and  $E_b$  are the energy gaps between the conduction and light-hole valence bands in the well and barrier materials, respectively. We solve the energy eigenvalues taking the band non-parabolicity into account according to Eqs. (1.15) and (1.16). Dealing with nonparabolicity is an iterative process. The energy eigenvalues depend on the masses which in turn depend on the energies. Therefore, the energy eigenvalues are initially calculated without considering the energy dependence of the masses. Subsequently, each of the energy values is fixed iteratively using the energy-dependent mass. Figure 1.5 describes the implementation of the band non-parabolicity in our models.

We have studied the effects of band non-parabolicity on the eigenenergy values and the results are shown in Fig. 1.6. In Fig. 1.6, the change in energy of the ground state due to non-parabolicity is plotted against well width for an  $\text{In}_{0.53}\text{Ga}_{0.47}\text{As}/\text{In}_{0.52}\text{Al}_{0.48}\text{As}$  single

quantum well structure.

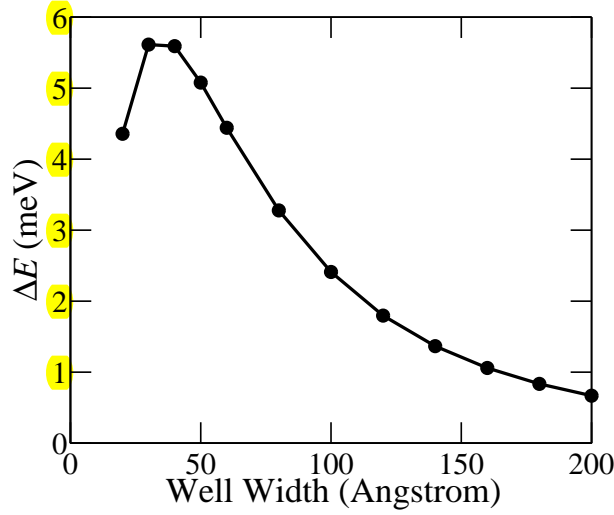


Figure 1.6: The difference in ground-state energy of an electron in a single  $\text{In}_{0.53}\text{Ga}_{0.47}\text{As}/\text{In}_{0.52}\text{Al}_{0.48}\text{As}$  quantum well, with and without non-parabolicity,  $\Delta E = E_1(\text{with non-parabolicity}) - E_1(\text{without non-parabolicity})$

## 1.4 Poisson's Equation

All of the techniques are now in place to be able to solve the Schrödinger equation for any heterostructure for which the band-edge potential profile defining the structure is known. However, all of the theoretical methods and examples described so far have concentrated solely on solving systems for a single charge carrier. In many devices such models would be inadequate as large numbers of charge carriers, *e.g.*, electrons, can be present in the conduction band, generating an additional electrostatic potential. In order to determine this additional potential  $V_\rho$  that will add to the usual band-edge potential term in the conduction band,  $V_{\text{CB}}$ , or, in the valence band,  $V_{\text{VB}}$ , one must solve Poisson's equation.

### 1.4.1 Calculating $V_\rho(z)$

In a doped semiconductor, there are two contributions to the charge density  $\sigma(z)$ ; first, there are the ionized impurities, and second, there are the free charge carriers. While the ionized

impurities can be known from the doping density in the semiconductor layers, as defined at growth time, the free charge carriers can be calculated from the probability distributions of the carriers in the quantum layers. Thus if  $D(z)$  defines the volume density of the dopants at position  $z$ , where the planes are separated by the usual step length  $\Delta z$ , then the total number of carriers, per unit cross-sectional area, introduced into the heterostructure is given by

$$N_d = \sum_{j=1}^N D(z_j). \quad (1.17)$$

Accordingly, if the carriers are distributed only in one state  $\psi$ , the net charge density in a plane can be written as

$$\sigma(z_j) = q[N_d\psi^*(z_j)\psi(z_j) - D(z_j)]\Delta z, \quad (1.18)$$

where  $q$  is the electronic charge. However, if the charge carriers are distributed over more than one subband, then the contributions to the charge density  $\sigma(z_j)$  have to be summed over the relevant subbands, *i.e.*,

$$\sigma(z_j) = q \left[ \sum_{i=1}^M N_{d,i} \psi_i(z_j)^* \psi_i(z_j) - D(z_j) \right] \Delta z, \quad (1.19)$$

where  $M$  is the number of subbands.

The additional potential term  $V_\rho(z)$  arising from the charge distribution  $\sigma(z)$ , can be expressed by using Poission's equation

$$V_\rho(z_j) = - \sum_{i=1}^j \sum_{i=1}^j \frac{\sigma(z_i)}{\epsilon(z_i)} \Delta z, \quad (1.20)$$

where  $\epsilon$  is the permittivity of the material, *i.e.*,  $\epsilon(z) = \epsilon_r(z)\epsilon_0$ .

Figure 1.7(a) shows the areal charge density,  $\sigma(z)$  along the growth axis for a 100 Å GaAs well,  $n$ -type doped to  $2 \times 10^{18} \text{ cm}^{-3}$ , surrounded by 200 Å undoped  $\text{Ga}_{0.8}\text{Al}_{0.2}\text{As}$  barriers. Figure 1.7(b) shows the additional electric field,  $\mathcal{E}(z)$  along the growth axis of the heterostructure due to  $\sigma(z)$ . The zero electric field at both ends implies charge neutrality in the structure. In addition, the zero field point at the center of the structure reflects the symmetry of the charge distribution. Figure 1.8(a) shows the potential as calculated from Eq. (??). The symmetry of the original heterostructure and doping profiles are reflected in

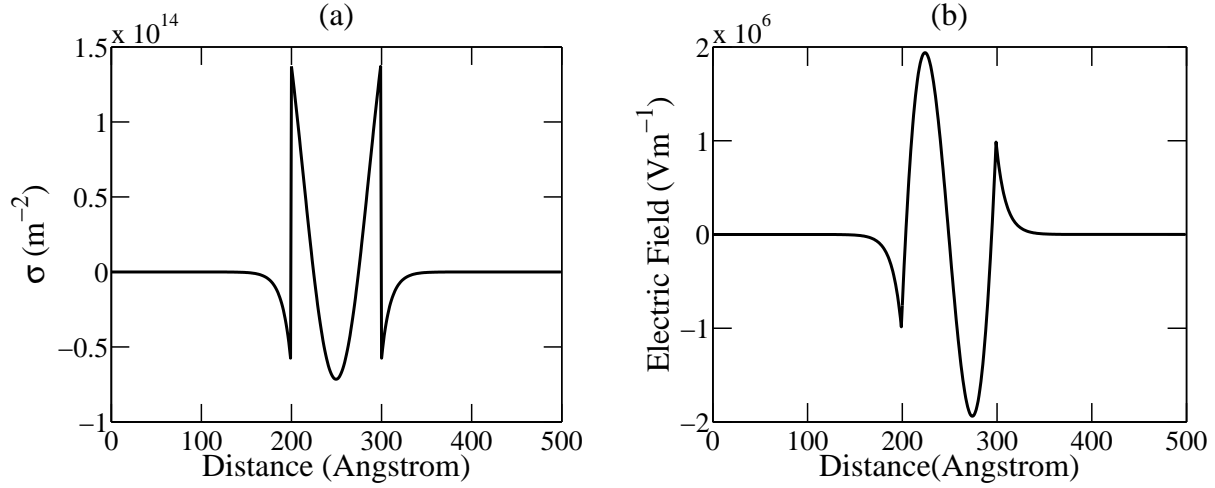


Figure 1.7: (a) Areal charge density and (b) Corresponding electric field for a 100 Å GaAs well,  $n$ -type doped to  $2 \times 10^{18} \text{ cm}^{-3}$ , surrounded by undoped  $\text{Ga}_{0.8}\text{Al}_{0.2}\text{As}$  barriers

the symmetric potential. The potential is positive at the center of the well since the system under consideration consists of electrons in the conduction band, so any test charge used to probe the potential is also an electron which would be repelled by the existing charge. The carrier density in this single quantum well is relatively high at  $2 \times 10^{12} \text{ cm}^{-2}$ , and produces a potential of up to 4 meV, while still is small compared to the conduction band offset, which is usually on the order of one or two hundred meV or more. Nonetheless, it is sufficient to have a measurable effect on the energy eigenvalues of the quantum well.

### 1.4.2 Self-consistent Schrödinger-Poisson Solution

For a complete determination of the eigenvalues and eigenvecotrs, the additional potential due to the carrier density is included in the standard Schrödinger equation, *i.e.*, the potential term  $V(z)$  in equation (1.8) becomes  $V_{\text{CB}} + V_{\rho}(z)$ . Figure 1.8(b) shows the conduction band-edge potential after  $V_{\rho}$  is added to  $V_{\text{CB}}$ . The perturbation, even at this relatively high carrier density of  $2 \times 10^{12} \text{ cm}^{-2}$ , remains small compared to the barrier height.

The numerical method, described in detail earlier, can be used without alteration to solve for this new potential, which will thus yield new energies and wavefunctions. The wavefunctions are important since the potential due to the charge distribution is itself dependent on the wavefunctions. Therefore, it is necessary to use an iterative approach solving

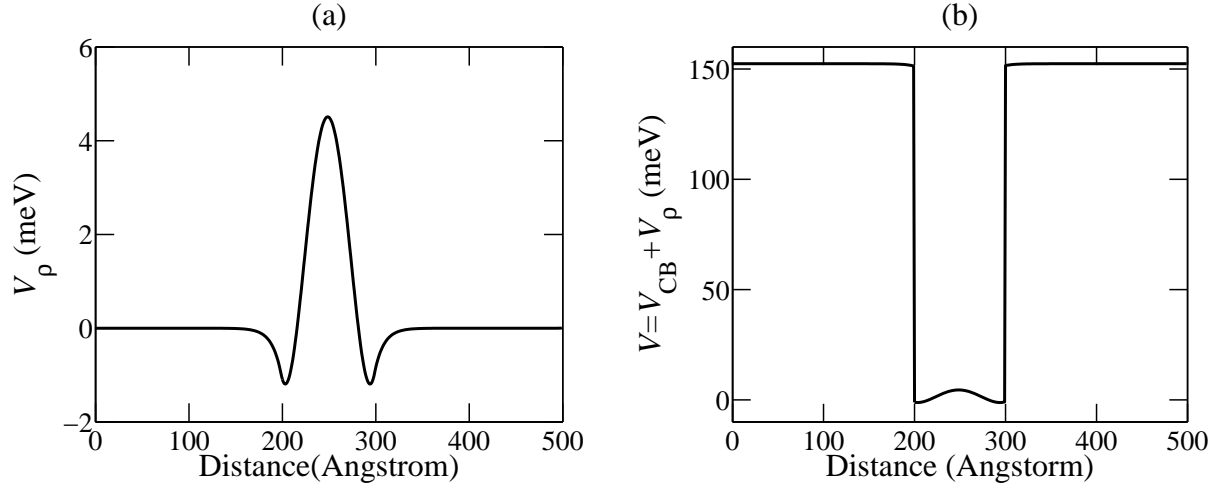


Figure 1.8: (a) Potential distrubutsion due to the ionised donor/electron charge distribution (b) The sum of the band-edge potential  $V_{CB}$  and Poission's potential  $V_\rho$  for the single quantum well of Fig. 1.7

Schrödinger's equation, calculating the potential due to the resulting charge distribution, adding it to the original band-edge potential, solving Schrödinger's equation again, and so on until convergence is reached. Figure 1.9 illustrates the way to solve the system taking the additional charge density into account.

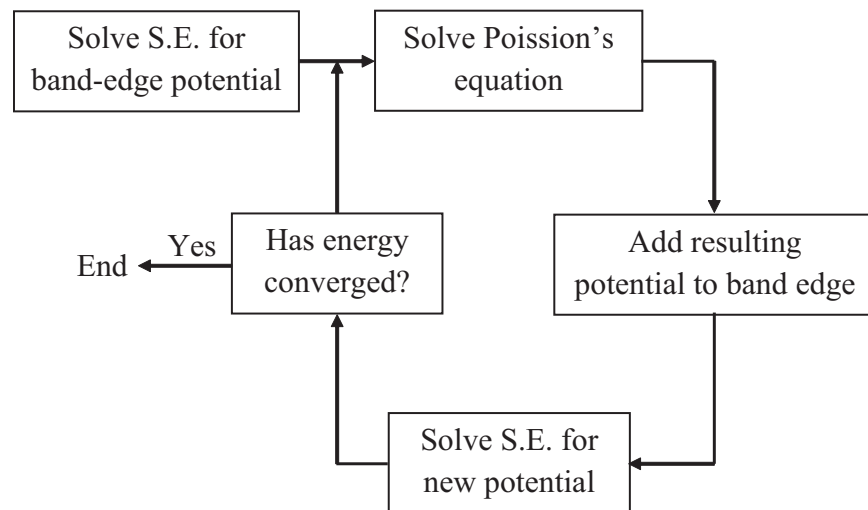


Figure 1.9: Block diagram illustrating the process of self-consistent iteration

# Chapter 2

## Intersubband Transitions

### 2.1 Dipole Matrix Element

Dipole matrix element between two subbands represent the strength of an optical transition between them. Generally, the definition of the dipole matrix element between two states  $i$  and  $f$  is

$$z_{if} = \langle \psi_i | z | \psi_f \rangle. \quad (2.1)$$

However, we must solve a one-dimensional Schrödinger equation, which includes the energy dependent effective mass

$$m^*(E) = m^*(E = 0) \left( 1 + \frac{E - V}{E_G} \right), \quad (2.2)$$

where  $(E - V)$  is the energy of the electron  $E$  measured from the conduction band edge  $V(z)$  of the material.

As a consequence, the wavefunctions that we compute with this approach are not orthogonal, which makes the definition of the dipole matrix element between the states  $i$  and  $f$  somewhat problematic [7]. The solution to this problem is to go back to the two-band model and compute the matrix element including the valence band part. Then the dipole matrix element can be written as [8]

$$z_{if} = \frac{\hbar}{2(E_f - E_i)} \left\langle \psi_i \left| p_z \frac{1}{m^*(E_i, z)} + \frac{1}{m^*(E_f, z)} p_z \right| \psi_f \right\rangle, \quad (2.3)$$



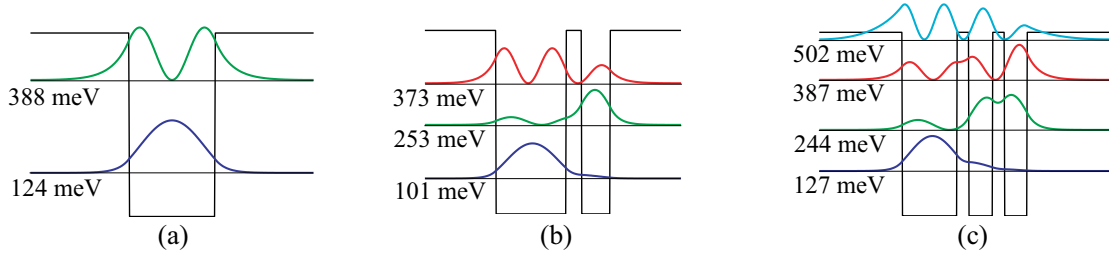


Figure 2.1: The bound states and energy levels in (a) single quantum well of 52 Å, (b) two coupled quantum wells: thick well 59 Å, thin barrier 13 Å, thin well 24 Å, and (c) three coupled quantum wells of 46 Å, 20 Å, 19 Å, barriers 10 Å.

where the momentum operator  $p_z$  is defined, as usual,  $p_z = -i\hbar\partial/\partial z$ . To account for the underlying valence band component, the wave functions  $\psi_i$  and  $\psi_f$  must be normalized according to [7]

$$1 = \left\langle \psi_i \left| 1 + \frac{E - V(z)}{E - V(z) + E_G(z)} \right| \psi_f \right\rangle. \quad (2.4)$$

We have calculated the bound energy levels and the dipole matrix elements for the single, double, and triple quantum wells studied by Sirtori, *et al.* [8]. The heterostructures consist InAlAs/InGaAs compounds. The calculated energy values and the moduli-squared wavefunctions are given in Fig. 2.1. We have compared our calculated values with the values reported by Sirtori, *et al.* [8]. The comparison is given in Table 2.

Quantum Wells	Energy Values (meV)		$\langle z_{if} \rangle (\text{\AA})$		
	Sirtori	Us	Experiment	Sirtori	Us
Single	123, 381	124, 388	15.3	14.8	14.17
Double	102, 252, 373	101, 253, 373	16.4	16.5	16.36
Triple	126, 242, 383, 494	127, 244, 387, 502	18.6	18.4	18.56

Table 2. Comparison of the energy and dipole matrix element values.

## 2.2 Nonradiative Transitions

### 2.2.1 Fermi's Golden Rule

The scattering rate for an electron initially in state  $|i, k_i\rangle$  (subband  $i$ , in-plane wavevector  $k_i$ ) to the final state  $|f, k_f\rangle$  through an interaction potential  $H'$  is evaluated using Fermi's Golden rule

$$W_{i \rightarrow f}(k_i, k_f) = \frac{2\pi}{\hbar} \left| \langle f, k_f | H' | i, k_i \rangle \right| \delta[E_f(k_f) - E_i(k_i)]. \quad (2.5)$$

The envelope wavefunctions  $\psi_i(z)$  and  $\psi_f(z)$  are obtained from the numerical integration of the coupled one-dimensional Schrödinger and one-dimensional Poisson differential equations as described earlier in Chap. 1.

### 2.2.2 Polar Longitudinal Optical (LO) Phonon Scattering

The electron-LO-phonon scattering rate can be written as

$$W_{i \rightarrow f}(k_i, k_f) = \frac{2\pi}{\hbar} \left| \langle f, k_f | H'_{\text{e-ph}} | i, k_i \rangle \right| \delta(E_f(k_f) - E_i(k_i) \pm \hbar\omega_{\text{LO}}), \quad (2.6)$$

where  $\hbar\omega_{\text{LO}}$  is the LO-phonon energy and  $H'_{\text{e-ph}}$  is the electron-LO-phonon interaction hamiltonian. The  $H'_{\text{e-ph}}$  can be given by [9]

$$H'_{\text{e-ph}} = \sum_{\mathbf{q}} [\alpha(\mathbf{q}) (e^{i\mathbf{q}\cdot\mathbf{r}} b_{\mathbf{q}} + e^{-i\mathbf{q}\cdot\mathbf{r}} b_{\mathbf{q}}^\dagger)], \quad (2.7)$$

where  $\alpha(\mathbf{q})$  is the electron-phonon interaction and  $b_{\mathbf{q}}$  and  $b_{\mathbf{q}}^\dagger$  are the creation and annihilation operators for a phonon in mode  $\mathbf{q}$ . The Fröhlich interaction strength for electron-polar-optical-phonon scattering is given by [10]

$$|\alpha(\mathbf{q})|^2 = \frac{\hbar\omega_{\text{LO}}}{2} \frac{e^2}{q^2} \left( \frac{1}{\epsilon_\infty} - \frac{1}{\epsilon_{\text{dc}}} \right), \quad (2.8)$$

where  $\epsilon_{\text{dc}}$  and  $\epsilon_\infty$  are the static and high frequency permittivities. The  $q^{-2}$  dependence of this term reduces scattering rates when large in-plane momentum transfers are required. This reduces scattering between subbands with a large energy separation.

The matrix element is given by [9]

$$\begin{aligned} \left| \langle f, k_f | H'_{\text{e-ph}} | i, k_i \rangle \right|^2 &= \frac{e^2 \hbar \omega_{\text{LO}}}{2V} \left( \frac{1}{\epsilon_{\infty}} - \frac{1}{\epsilon_{\text{dc}}} \right) \frac{1}{q_z^2 + q_{\parallel}^2} |A_{i \rightarrow f}|^2 \\ &\times \delta_{k_i, k_f \mp q_{\parallel}} (n_{\omega_{\text{LO}}} + 1/2 \mp 1/2), \end{aligned} \quad (2.9)$$

where  $\mathbf{q}_{\parallel}$  and  $\mathbf{q}_z$  are the components of the phonon wavevector that are perpendicular (in-plane) and parallel to the growth axis ( $\hat{z}$ ) respectively,  $n_{\omega_{\text{LO}}}$  is the Bose-Einstein occupation, and the upper and lower signs correspond to phonon absorption and emission respectively.

The delta function ensures in-plane momentum conservation, and the form factor

$$A_{i \rightarrow f}(q_z) = \int_{-\infty}^{\infty} dz \psi_f^*(z) \psi_i^*(z) e^{\pm q_z z} \quad (2.10)$$

is related to the  $q_z$  momentum uncertainty due to the spatially localized envelope wavefunctions  $\psi_i(z)$  and  $\psi_f(z)$ .

This expression can then be integrated over the phonon modes  $\mathbf{q}$  and final states  $\mathbf{k}_f$  to yield the scattering rate from an initial wavevector  $W(\mathbf{k}_i)$ . Assuming parabolic subband dispersion, the final states lie on a circle with radius  $k_f$  determined by conservation of energy.

$$k_f^2 = k_i^2 + \frac{2m^*(E_f(0) - E_i(0) \mp \hbar \omega_{\text{LO}})}{\hbar^2}. \quad (2.11)$$

Energy conservation and the in-plane momentum conservation rule allows us to write the phonon wavevector  $\mathbf{q}_{\parallel}$  in terms of  $\mathbf{k}_i$  and  $\mathbf{k}_f$ :

$$q_{\parallel}^2 = |\mathbf{k}_i - \mathbf{k}_f|^2 = k_i^2 + k_f^2 - 2k_i k_f \cos \theta, \quad (2.12)$$

where the angle  $\theta$  is the angle between the in-plane wavevectors  $\mathbf{k}_i$  and  $\mathbf{k}_f$ . After summation over the phonon modes  $\mathbf{q}$ , Eq. (2.6) can be integrated over these final states  $\mathbf{k}_f$  to yield the total scattering rate from an initial wavevector:

$$W_{i \rightarrow f}^{\text{abs}}(k_i) = \frac{m^* e^2 \omega_{\text{LO}}}{8\pi \hbar^2} \left( \frac{1}{\epsilon_{\infty}} - \frac{1}{\epsilon_{\text{dc}}} \right) n_{\omega_{\text{LO}}} \int_0^{2\pi} d\theta B_{i \rightarrow f}(q_{\parallel}), \quad (2.13)$$

$$W_{i \rightarrow f}^{\text{em}}(k_i) = \frac{m^* e^2 \omega_{\text{LO}}}{8\pi \hbar^2} \left( \frac{1}{\epsilon_{\infty}} - \frac{1}{\epsilon_{\text{dc}}} \right) (n_{\omega_{\text{LO}}} + 1) \int_0^{2\pi} d\theta B_{i \rightarrow f}(q_{\parallel}), \quad (2.14)$$

where  $B_{i \rightarrow f}$  is given by

$$B_{i \rightarrow f} = \int_{-\infty}^{\infty} dz \int_{-\infty}^{\infty} dz' \psi_f^*(z) \psi_i(z) \psi_i^*(z') \psi_f(z') \frac{1}{q_{\parallel}} e^{-q_{\parallel} |z - z'|}. \quad (2.15)$$

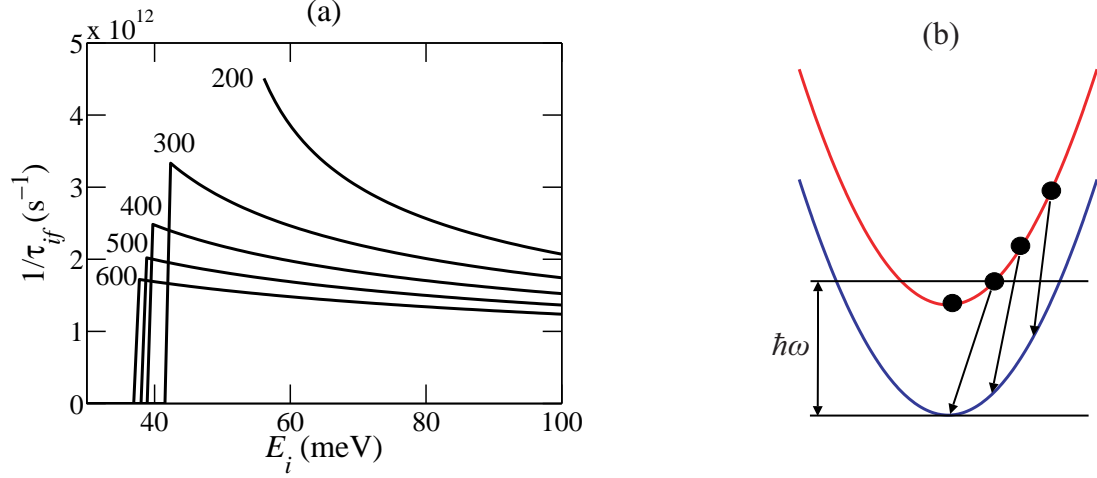


Figure 2.2: (a) The scattering rate for a variety of well widths (in Å) (b) The effect of the LO phonon energy cut-off on intersubband electron scattering

The total scattering time between subbands  $\tau_{i \rightarrow f}$  can then be obtained by averaging over all possible initial states in the subband [11]

$$\frac{1}{\tau_{i \rightarrow f}} = \frac{\int_0^\infty dE_k f_i(E_k) [1 - f_f(E_k \mp \hbar\omega_{LO})] W_{i \rightarrow f}(E_k)}{\int_0^\infty dE_k f_i(E_k)}, \quad (2.16)$$

where  $E_k = \hbar^2 k_{\parallel}^2 / 2m^*$  is the in-plane kinetic energy in the initial subband, and  $f_i(E_k)$  is the Fermi distribution in the initial state and  $f_f(E_k)$  is the Fermi distribution in the final state. Non-equilibrium subband distributions can be dealt with by assigning different quasi-Fermi levels and electron temperatures for the initial and final Fermi distributions.

In Fig. 2.2(a), we illustrate the scattering rate due to LO phonon emission for an electron initially in the first excited subband and finally in the ground subband of an infinitely deep GaAs quantum well. We assume that the electrons are at the same temperature of the lattice, which is 77 K. For quantum well widths greater than 300 Å, the scattering rate falls rapidly to zero below a threshold initial energy value, indicating that the subband separation,  $E_2 - E_1$ , becomes less than the LO phonon energy. The cut-off in the scattering rate occurs when the electrons in the upper subband do not have sufficient energy to emit an LO phonon, and hence are unable to scatter. This feature is also schematically illustrated in Fig. 2.2(b). Moving from the upper right down the curve, electrons have sufficient kinetic energy which, when combined with the potential energy of the upper subband, allows them

to emit a phonon; however, the third electron represents the minimum kinetic energy for scattering. Below this point, the electrons are less than an LO phonon away from the energy minimum of the *complete* system and hence cannot scatter.

Figure 2.3 shows calculated average scattering rates via LO phonon emission from subband 2 to subband 1 using Eq. (2.16) in a GaAs infinitely deep quantum well. The well-width is varied to illustrate the effect of energy spacing between the minima of the subbands,  $E_{21} = E_2 - E_1$ . In this calculation, we assume that the electron density in each subband is  $10^{10} \text{ cm}^{-2}$ . We also assume that the electrons have a temperature equal to that of the lattice. In Fig. 2.3, as the subband separation decreases, the scattering rate increases up to almost a *resonance* point and then decreases rapidly. As may be expected for fixed phonon energy, which is 36 meV for GaAs, the peak in the scattering rate occurs when the subband separation is equal to the phonon energy.

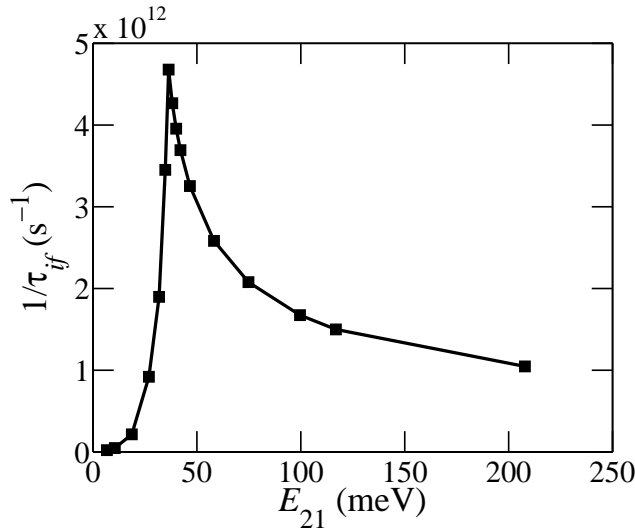


Figure 2.3: The mean scattering rate averaged over distributions in both the initial and final subbands vs. the subband separation

In case of LO phonon absorption, the density of phonons in the medium plays a significant role. The phonon density increases as the temperature rises, thus increasing the probability of an absorption. Figure 2.4 shows the ratio of the LO phonon emission to absorption rate between the first excited and ground states in an infinite GaAs quantum well. The emission rate is always greater than the absorption rate.

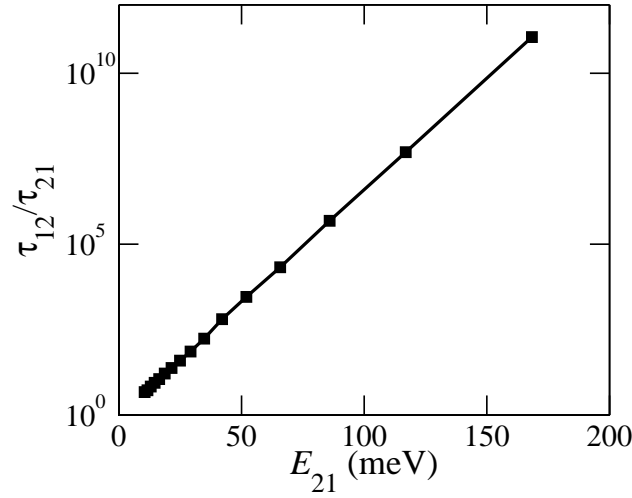


Figure 2.4: The ratio of the mean electron-LO phonon emission ( $1/\tau_{21}$ ) to absorption ( $1/\tau_{12}$ ) rate vs. the subband separation

### 2.2.3 Electron-Electron Scattering

Accurate calculation of electron-electron scattering rates in quantum well systems is a theoretically complicated many-body problem. There is a much greater variety of scattering mechanisms possible than in the essentially one-body problem encountered in phonon scattering. Figure 2.5 illustrates all of the possible mechanisms in a two-level system, where at least one of the carriers changes its subband, these are usually referred to as *inter-subband* transitions. The second in Fig. 2.5 illustrates the symmetric inter-subband event,  $22 \rightarrow 11$  which moves two carriers down a level. The first and third in Fig. 2.5 show Auger-type

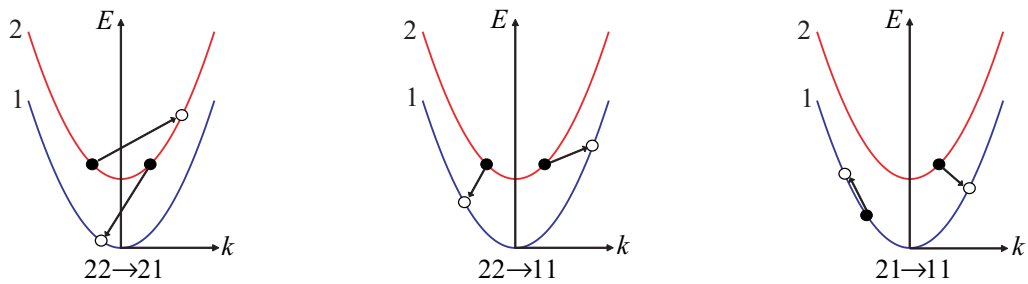


Figure 2.5: Illustration of various intersubband carrier-carrier scattering mechanisms in a two-level system

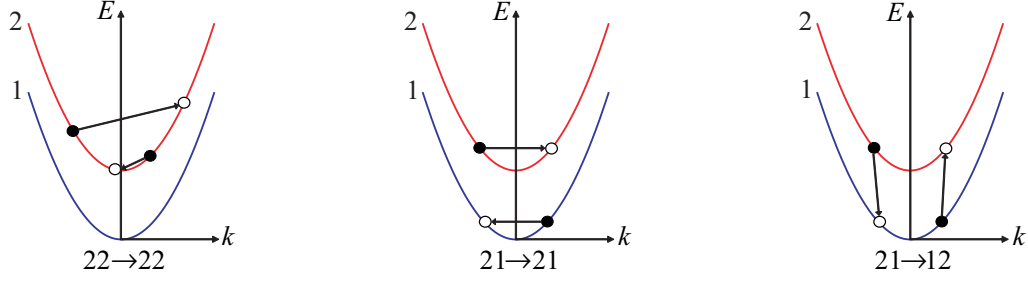


Figure 2.6: Illustration of various ‘intrasubband’ carrier-carrier scattering mechanisms in a two-level system

inter-subband scattering, where one carrier relaxes down to a lower subband, giving its excess energy to another carrier which remains within its original subband. In addition to the above, there are also scattering events where the number of carriers in each subband does not change. Some of these are illustrated schematically in Fig. 2.6

Electron-electron interaction is mediated by the coulomb potential, which is screened by the surrounding electron system. In low density systems where the single particle picture is applicable, Fermi’s Golden Rule is the most common method for calculating scattering rates. Because of the mathematical complexity of describing screening in a multi-subband system at finite temperature, simplified models are typically used and calculations show that for moderate densities ( $< 5 \times 10^{11} \text{ cm}^{-2}$ ), there is little difference between intersubband rates calculated with and without screening [12].

An electron in subband  $i$  with wavevector  $\mathbf{k}_i$  scattering with another electron in subband  $j$  with wavevector  $\mathbf{k}_j$ , where the electrons end up in subbands  $f$  and  $g$  with wavevectors  $\mathbf{k}_f$  and  $\mathbf{k}_g$  respectively. The unscreened matrix element for this event is

$$H'_{i,j \rightarrow f,g}(\mathbf{k}_i, \mathbf{k}_j, \mathbf{k}_f, \mathbf{k}_g) = \frac{2\pi e^2}{S_{\parallel} \epsilon} A_{i,j \rightarrow f,g}(q_{\parallel}) \delta(\mathbf{k}_f + \mathbf{k}_g - \mathbf{k}_i - \mathbf{k}_j), \quad (2.17)$$

where

$$q_{\parallel} = |\mathbf{k}_i - \mathbf{k}_f|, \quad (2.18)$$

and the form factor is

$$A_{i,j \rightarrow f,g}(q_{\parallel}) = \int_{-\infty}^{\infty} dz \int_{-\infty}^{\infty} dz' \psi_i(z) \psi_f^*(z) \psi_j(z') \psi_g^*(z') e^{-q_{\parallel} |z - z'|}. \quad (2.19)$$

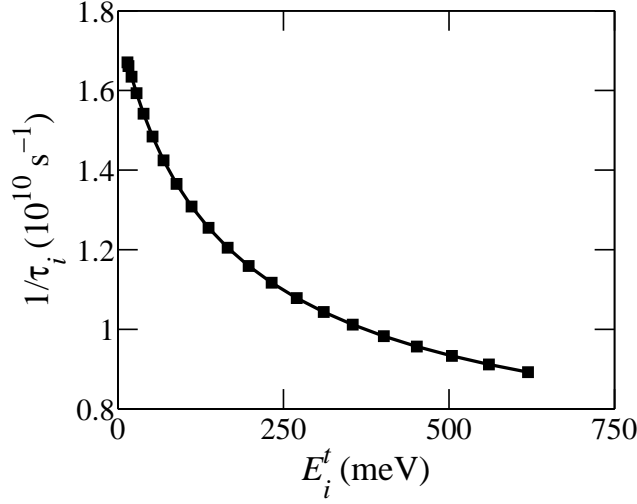


Figure 2.7: The electron–electron scattering rate as a function of the initial electron energy

Then the total e-e scattering rate is given by [9]

$$W_{i,j \rightarrow f,g}(\mathbf{k}_i) = \frac{e^4}{2\pi\hbar\epsilon^2} \int d^2\mathbf{k}_j \int d^2\mathbf{k}_f \int d^2\mathbf{k}_g \frac{|A_{i,j \rightarrow f,g}(q_{\parallel})|^2}{\epsilon_{sc}^2(q_{\parallel}, T)q_{\parallel}^2} f_{j,\mathbf{k}_j}(1 - f_{g,\mathbf{k}_g})(1 - f_{f,\mathbf{k}_f}) \\ \times \delta(E_f(\mathbf{k}_f) + E_g(\mathbf{k}_g) - E_i(\mathbf{k}_i) - E_j(\mathbf{k}_j))\delta(\mathbf{k}_f + \mathbf{k}_g - \mathbf{k}_i - \mathbf{k}_j), \quad (2.20)$$

where  $\epsilon_{sc}^2(q_{\parallel}, T)$  represents the correction due to the dielectric constant resulting from screening. The total scattering time  $\tau_i$  can then be obtained by averaging over all possible initial states in the subband

$$\frac{1}{\tau_i} = \frac{\int_0^\infty dE_k^i f_i(E_k^i) W_{i,j \rightarrow f,g}(E_k^i)}{\int_0^\infty dE_k^i f_i(E_k^i)}, \quad (2.21)$$

Figure 2.7 shows the results of a calculation of the  $22 \rightarrow 11$  electron–electron scattering rate as a function of the electron energy of the initial state  $i$  in an infinitely deep 400 Å wide GaAs quantum well. We assume that the electron temperature is 77 K and the electron density is  $10^{10} \text{ cm}^{-2}$ . The effect of increasing carrier density is shown in Fig. 2.8. The range of carrier densities has been chosen to span roughly those found in intersubband devices. It can be seen that with this model the intersubband electron-electron scattering is almost proportional to the carrier density.



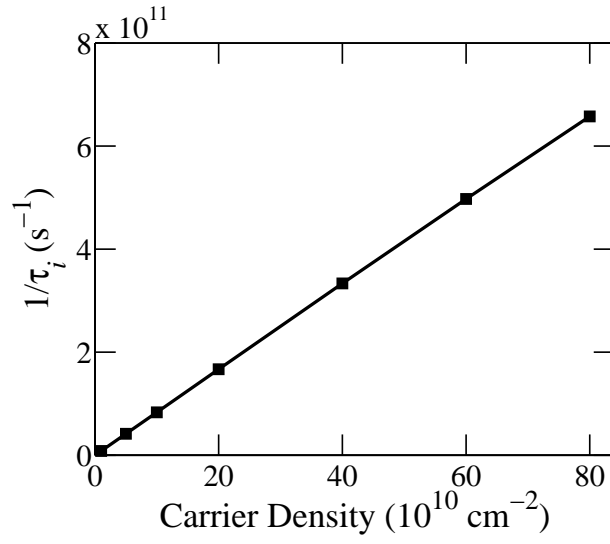


Figure 2.8: The mean 22→11 electron–electron scattering rate as a function of the carrier density in state  $|2\rangle$ , for a 400 Å infinitely deep quantum well at 77 K

# Bibliography

- [1] G. Bastard, *Wave Mechanics Applied to Semiconductor Heterostructures*, John Wiley & Sons, New York (1988).
- [2] The Mathworks, Inc. <http://www.mathworks.com>.
- [3] P. Harrison, *Quantum wells, wires and dots*, 2nd Ed., Wiley (2005).
- [4] D. F. Nelson, R. C. Miller, and D. A. Kleinman, “Band nonparabolicity effects in semiconductor quantum wells,” *Phys. Rev. B* **35**, 7770 (1987).
- [5] G. Bastard, “Theoretical investigations of superlattice band structure in the envelope-function approximation,” *Phys. Rev. B* **25**, 7584 (1982).
- [6] G. Bastard, “Superlattice band structure in the envelope-function approximation,” *Phys. Rev. B* **24**, 5693 (1981).
- [7] J. Faist, F. Capasso, C. Sirtori, D. Sivco, and A. Cho, *Intersubband Transitions in Quantum Wells: Physics and Device Applications II*, Academic Press, Ch. 1, p. 6-7 (2000).
- [8] C. Sirtori, F. Capasso, and J. Faist, “Nonparabolicity and a sum rule associated with bound-to-bound and bound-to-continuum intersubband transitions in quantum wells,” *Phys. Rev. B* **50**, 8663 (1994).
- [9] J. H. Smet, C. G. Fonstad, and Q. Hu, “Intrawell and interwell intersubband transitions in multiple quantum wells for far-infrared sources,” *J. Appl. Phys.* **79**, 9305 (1996).

- [10] P. J. Price, “Two-dimensional electron transport in semiconductor layers. I. phonon scattering,” *Ann. Phys. (N.Y.)* **133**, 217 (1981).
- [11] S.-C. Lee, I. Galbraith, and C. R. Pidgeon, “Influence of electron temperature and carrier concentration on electron-LO-phonon intersubband scattering in wide GaAs/Al<sub>x</sub>Ga<sub>1-x</sub>As quantum wells,” *Phys. Rev. B* **52**, 1874 (1995).
- [12] S.-C. Lee and I. Galbraith, “The intrasubband and intersubband relaxation of nonequilibrium electron populations in wide semiconductor quantum wells,” *Physica E* **7**, 229 (2000).